Large Area, High Resolution Mapping of Approximate Rotational Symmetries in a $Pd_{77.5}Cu_6Si_{16.5}$ Metallic Glass Thin Film

Shuoyuan Huang [a], Carter Francis [a], John Sunderland [a], Vrishank Jambur [a], Izabela Szlufarska [a], Paul M Voyles [a, *]

[a] Department of Materials Science and Engineering, University of Wisconsin Madison, Madison, Wisconsin 53706, USA

* paul.voyles@wisc.edu

Abstract Densely spaced four-dimensional scanning transmission electron microscopy (4D STEM) analyzed using correlation symmetry coefficients enables large area mapping of approximate rotational symmetries in amorphous materials. Here, we report the effects of Poisson noise, limited electron counts, probe coherence, reciprocal space sampling, and the probe-sample interaction volume on 4D STEM symmetry mapping experiments. These results lead to an experiment parameter envelope for high quality, high confidence 4D STEM symmetry mapping. We also establish a direct link between the symmetry coefficients and approximate rotational symmetries of nearest-neighbor atomic clusters using electron diffraction simulations from atomic models of a metallic glass. Experiments on a $Pd_{77.5}Cu_6Si_{16.5}$ metallic glass thin film demonstrate the ability to image the types, sizes, volume fractions, and spatial correlations amongst local rotationally symmetry regions in the glass.

Keywords: 4D STEM; Correlation symmetry analysis; Amorphous structure; Short- and medium-ranged order

1. Introduction

Glasses lack long range periodicity, but they have well-defined short- and medium-range order (SRO and MRO). In metallic glasses, Voronoi polyhedra (VPs) [1], Frank-Kasper tetrapolyhedra [2], and Z-clusters [3] are example SRO motifs. Packing of these local motifs leads to MRO that can (for example) contain icosahedral or crystal-like symmetry structures [4–7]. The types of these clusters in the glass structure influence the glass forming ability [8], dynamics [9,10], and mechanical properties [11] of the alloy, so it is important to identify the SRO and MRO in metallic glasses.

Ordered clusters in amorphous materials can be identified experimentally using electron microscopy. Fluctuation electron microscopy (FEM) uses coherent electron diffraction to probe the statistical variance of local structures in different volumes [12]. Stratton and Voyles [13] developed a quantitative model for variable resolution FEM (VR-FEM) which assumes the structure of the sample as a nanocrystal / amorphous matrix composite. This model can determine the size and volume fraction of the nanocrystals from a VR-FEM experiment, but it does not account for non-crystal-like ordering. Hybrid reversed Monte Carlo (HRMC) simulations have been used to construct atomistic models in agreement with FEM measurements [6,7]. The structural models can be further characterized using metrics such as VP.

Local rotational symmetries in electron nanodiffraction (END) patterns, which reflect rotational symmetries in the structure, provide a more direct observation of local clusters [14]. The rotational symmetry in END patterns has been evaluated by the angular correlation function of the intensity and its power spectrum. These analyses capture the magnitude of symmetry of different rotational order and at different wave vectors [15], but interpreting the power spectrum requires complex statistical analysis [16], and it can be susceptible to non-structural features [17]. Inspired by the Symmetry STEM method of Kranjak and

Etheridge [18], we recently proposed correlation symmetry analysis as an improved method to extract symmetries from END experiments on amorphous samples [17]. Instead of calculating the angular power spectrum, correlation symmetry analysis averages the correlations at the characteristic angles of rotational symmetries. Symmetry coefficients can be more robust against multiple scattering and non-Friedel symmetry in diffraction patterns than power spectrum analysis.

Any of the symmetry analysis methods can be extended to symmetry mapping by using a fast detector and densely-sampled 4D STEM data. Liu *et al*. [19] mapped symmetries in a small, 3 nm by 3 nm region of a $Zr_{36}Cu_{64}$ glass by collecting END patterns using a CCD camera. The magnitude of the power spectrum at a fixed wave vector and rotational order for each spatial pixel was used to create a spatial symmetry map. Comparison with simulated END data confirmed the local icosahedral order. The field of view and thus statistical power in that experiment was limited by the slow readout of the CCD camera. Im *et al.* [20] performed a 4D STEM experiment on a $Zr_{55}Co_{25}Al_{20}$ glass with a larger 40 nm by 40 nm field of view using a faster electron microscope pixel array detector (EMPAD) direct detector. This provides an estimate, albeit from a small region, of the sizes of the local clusters with different orders. Even faster cameras [21,22] are enabling densely spaced 4D STEM experiments on very large fields of view with high spatial sampling, although at low electron counts per END pattern.

Here, we report a systematic study of spatial symmetry mapping on amorphous samples using correlation symmetry analysis via densely spaced 4D STEM. First, we connect symmetry coefficients to VPs using multislice simulations of END data from atomistic models of Al-rare earth metallic glasses. Then, we discuss, using statistical models and experiments, the influence of experimental noise, electron counts, reciprocal space sampling and spatial coherence of the probe on the symmetry coefficient signal. These results lead to an operating envelope of experimental conditions for fast 4D STEM symmetry mapping. An example large area experiment on a $Pd_{77.5}Cu_6Si_{16.5}$ metallic glass thin film demonstrates the ability to measure the sizes, densities, and spatial correlations of local clusters with different symmetries.

2. Methods

4D STEM experiments were conducted on a Thermo-Fisher Scientific Titan microscope operated at 200 keV. The microscope was set in micro-probe STEM mode to create coherent nanometer-sized electron beams. Probes with semi-convergence angles of 0.7, 1.5, and 2.51 mrad and Rayleigh-criterion resolutions of 2.2, 1.0, and 0.6 nm were used to study the probe-sample interaction volume effect. A probe semi-convergence angle of 2.51 mrad was used for all other experiments. Probe currents of 1.6, 6.4, 25, and 102 pA, created by changing the microscope spot number from 9 to 3, were used to study the effect of probe coherence. A probe current of 6.4 pA was used for all other experiments.

The END patterns were collected by a Direct Electron DE-Celeritas camera. The frame rate was fixed at 20,000 fps for data collected to study the electron counts and probe-sample interaction volume. For data collected to study the probe coherence effect, different frame rates were used for different probe currents to maintain equal mean counts per pattern. Frames rates of 50, 100, 200, and 400 fps were used for probe currents from 1.6 to 102 pA. 1000 fps readout speed was used for large area symmetry mapping experiment. All experiments used 256 by 256 detector readout area. Camera length were set differently for experiments with different convergence angle to fit the first diffraction ring inside the detector. 48 mm camera length was used for 2.51 mrad probe and 77 mm camera length was used for 1.5 mrad and 0.7 mrad probes. Details about the scan controller system for 4D STEM scan acquisition can be found in [23]. 120 by 120 scanning array with step size of 0.52 nm were used for sparse sampling data collected to study the effect of electron counts, coherence, and probe-sample interaction volume. 1000 by 1000 scanning array with step size of 0.06 nm were used for dense sampling data collected for large area (62 nm by 62 nm) symmetry mapping.

$Pd_{77.5}Cu_6Si_{16.5}$ thin films were synthesized using single alloy target magnetron sputtering at room temperature. An arc-melted alloy target with nominal composition $Pd_{77.5}Cu_6Si_{16.5}$ was purchased from ACI Alloys. Deposition occurred inside a custom-built high vacuum chamber with an operating pressure less than 5×10^{-8} Torr and with a partial pressure of oxygen of 2×10^{-10} Torr and a partial pressure of water vapor of 5×10^{-9} Torr. A Tourus Magnetron sputtering gun from Kurt J Lesker was used to deposit the films onto electron transparent 15-nm-thick Si_3N_4 membranes with a deposition rate of 0.24 nm/s and an Ar process gas pressure of 3.1 mTorr. Two samples were prepared with nominal thicknesses of 10 and 20 nm by varying the deposition time.

END patterns were simulated from a set of $Al_{100-x}Sm_x$ atomistic models generated by molecular dynamics (MD) as described in [24]. To achieve better statistics from relatively small models, the models were rotated into 211 orientations even distributed on the top half of the unit orientation sphere, and END patterns were simulated in each orientation. Multislice simulations of the model were carried out using PRISMATIC [25]. A probe with semi-angle of 3.062 mrad at 200 keV energy was used with zero defocus and zero aberrations. The probe was scanned across the model with a step size of 0.5 nm to avoid overlapping. The multisilice potentials were calculated using 2.892 Å slice thicknesses. Ten frozen phonon configurations were averaged together for each END pattern. Standard deviations of 0.1 Å were used for both Al and Sm atoms thermal vibration in the frozen phonon configurations. The simulation supercells are one cell in thickness (58 Å).

The experimental and simulated 4D datasets were processed with correlation symmetry analysis implemented in the pyxem package [26]. Each pattern is first unwrapped into polar coordinates $I(k, \varphi)$. Then the Pearson correlation at angular shift Δ is calculated as

$$\rho(\Delta) = \frac{\langle I(k,\varphi)I(k,\varphi+\Delta)\rangle_{k,\varphi} - \langle I(k,\varphi)\rangle^2_{k,\varphi}}{\langle I(k,\varphi)^2\rangle_{k,\varphi} - \langle I(k,\varphi)\rangle^2_{k,\varphi}}, \quad (1)$$

where $\langle \dots \rangle_{k,\varphi}$ denotes averaging over wave vector k and azimuthal angle φ. The k averaging windows are chosen to reflect the k ranges of the first diffraction rings. For experimental $Pd_{77.5}Cu_6Si_{16.5}$ data, $\rho(\Delta)$ was averaged from 0.4 to 0.5 $Å^{-1}$. For the simulated $Al_{100-x}Sm_x$ dataset, three different windows were used due to the changes in the average interatomic distances with x. 0.375 to 0.415 $Å^{-1}$ were used for $Al_{94}Sm_6$, 0.37 to 0.41 $Å^{-1}$ for $Al_{92}Sm_8$, and 0.365 to 0.405 $Å^{-1}$ for $Al_{90}Sm_{10}$. The symmetry coefficients are calculated by

$$S(n) = \frac{1}{N}\sum_{i=1}^{N} \rho(\delta_i^n), \quad (2)$$

where δ_i^n's are the characteristic angles of the nth order rotational symmetry. In the simulated $Al_{100-x}Sm_x$ dataset, the symmetry coefficients at all probe positions for all rotations were averaged to generate an average $S(n)$. For sparse sampling experimental $Pd_{77.5}Cu_6Si_{16.5}$ data, the symmetry coefficients at all probe positions were averaged to generate the spatial averaged $S(n)$. For dense sampling $Pd_{77.5}Cu_6Si_{16.5}$ data, the rotational symmetries in each spatial pixel are represented as $S(x, y, n)$ to generate symmetry maps of different orders. All the averaging on $S(n)$'s were performed after positive truncation. More details about the correlation symmetry analysis can be found in [17].

3. Results and Discussion

3.1 Connecting Symmetry Coefficients to Atomistic Structure

The magnitude of symmetry coefficient $S(n)$ reflects the degree of n-fold symmetry in the diffraction pattern. Figure 1 shows that the symmetry coefficients also reflect the rotational symmetry of the atomistic structure. It shows the average 4- and 10-fold symmetry coefficients versus the percentages of crystal-like

and icosahedral-like VPs from three $Al_{100-x}Sm_x$ atomistic models with x = 6, 8, and 10. Crystal-like is defined as VPs with no less than 4 four-edged faces and with coordination number between 10 to 14, such as <0,4,4,4>. Icosahedral-like is defined as VP with more than 8 pentagon faces and with coordination number between 10 to 14, such as <0,0,12,0>, or <0,1,10,2>. Increasing x increases the icosahedral VP concentration and decreases the crystal-like VP concentration [24]. Models with more atoms in crystal-like configurations display higher orientation averaged $S(4)$, and models with more atoms in icosahedral-like configurations display higher orientation averaged $S(10)$. Although the models contain far more icosahedral VPs than crystal-like VPs, the magnitude of $S(10)$ is generally smaller than that of $S(4)$. This is because $S(10)$averages the Pearson correlation over more angles than $S(4)$, so it is more susceptible to cluster misorientation, distortion, and random overlapping of more than one cluster through the sample thickness. It is worth noting that the simulation boxes are only 5.8 nm thick, which is significantly thinner than the experimental samples studied here, although not thinner than some experimental samples[27]. As a result, these simulations contain fewer non-structural features, as will be discussed below.

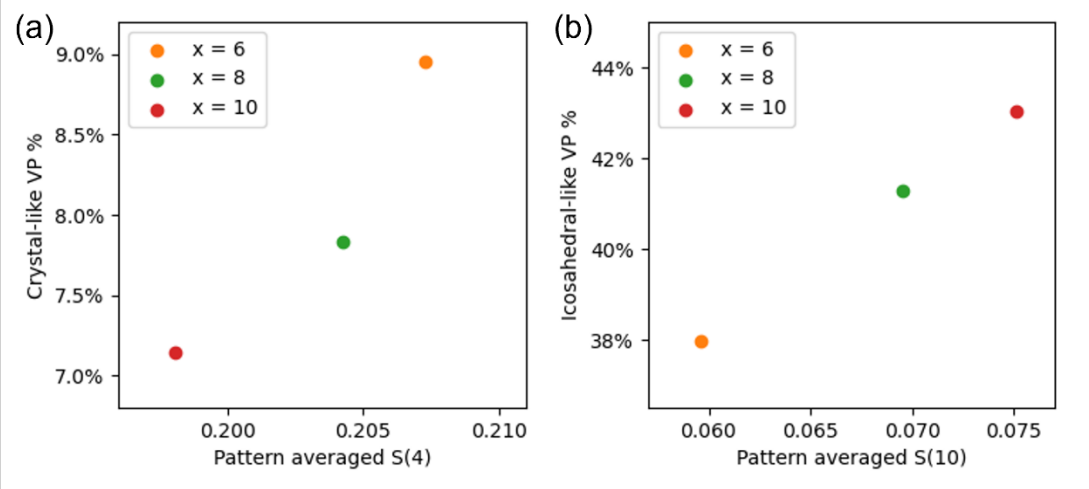

Figure 1. (a) Percentage of crystal-like VPs versus orientation averaged $S(4)$ for the three $Al_{100-x}Sm_x$ models; (b) percentage of icosahedral-like VPs versus orientation averaged $S(10)$ for the three $Al_{100-x}Sm_x$ models.

3.2 Experimental Conditions for Reliable Symmetry STEM Maps

In fast 4D STEM experiments, the main source of experimental noise is Poisson noise due to the low number of electrons in each END pattern. Poisson noise reduces the Pearson correlation coefficient at all angular shifts. As shown in Appendix A, the Poisson noise influenced symmetry coefficient can be written as

$$S_{n,\mathrm{exp}} = S_{n,0} \times \frac{1}{1 + 1/V_r I_r}, \tag{3}$$

where $S_{n,0}$ is the symmetry coefficient calculated from a noiseless pattern, I_r is the mean intensity of the pattern in the k window used to calculate symmetry coefficient, and $V_r = \langle I^2 \rangle / \langle I \rangle^2 - 1$ is the "ring" variance as defined in [28] measured without noise (or at infinite dose). We will call I_r the mean ring intensity and measure it in units of the number of electrons. (Eq. 3 is not correct if I_r is measured in units of digital counts.) Correction of the systematic error expressed in Eq. 3 is critical, as it depends on the "ring" variance which is structure dependent. Less structured glasses with lower V_r get more reduction in symmetry coefficient at fixed electron dose. The measured V_r at finite dose is in turn influenced by Poisson

noise via an additive term $V_{r,p} = 1/I_r$ [12], so a minimum number of electron counts is needed to reliably estimate V_r.

Simulated END patterns with artificial noise are used to demonstrate the effect of Poisson noise on the symmetry coefficients and the effectiveness of correction with Equation 3. The noiseless simulated END patterns were first scaled to different I_r, and then corrupted with randomly-generated Poisson noise. Figure 2 shows the orientation averaged $S(2)$ of simulations from the $Al_{94}Sm_6$ model at different I_r's. Inset images shows examples of noisy patterns at different I_r's with the same ground truth. Orientation averaged $S(n)$ diverges at low I_r both with and without noise correction.

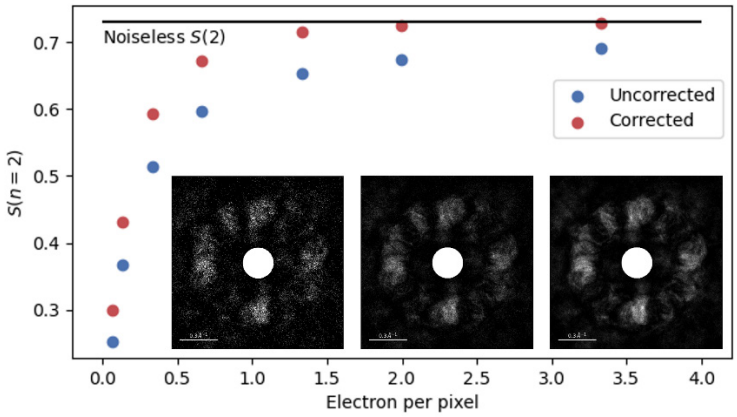

Figure 2. Orientation averaged $S(2)$ of $Al_{94}Sm_6$ model calculated from a simulated dataset corrupted by Poisson noise at different mean ring intensities before (blue) and after (red) noise correction. $S(2)$ for the ground truth, noiseless data is 0.731, as marked by the black line. The insets are examples of the same simulation patterns added with Poisson noise at different electron counts. Scale bars are 0.3 $Å^{-1}$.

To access the performance of noise correction at limited electron intensity, both corrected and uncorrected $S(n)$ can be fit to a function of the form $S(I_r) = S_0/(1 + a/I_r)$, where a and S_0 are fitting parameters. S_0 can be treated as the converged value at infinitely large mean ring intensity, *i.e.*, the noiseless symmetry coefficient, and we can define a minimum I_r required to obtain $S(I_r)$ within some percentage of S_0. Table 1 shows the thresholds using 5% and 10% deviation as criteria calculated from simulated data both with and without noise correction. Noise correction using Eq. 3 gives quantitatively reliable $S(2)$ at about 20% lower counts in the END patterns for this simulated dataset.

Table 1. Threshold mean ring intensities I_r (electrons per pixel) calculated from simulation and experiment before and after noise correction under two criteria.

Criteria	Simulation		Experiment	
	Uncorrected	Corrected	Uncorrected	Corrected
10% Deviation in S(n)	1.13	0.90	7.40 ± 0.02	1.04 ± 0.4
5% Deviation in S(n)	2.40	1.91	15.6 ± 0.04	2.20 ± 0.9

Figure 3 shows experimental $S(2)$ as a function of I_r, both corrected and uncorrected. The data were collected from a 20 nm thick $Pd_{77.5}Cu_6Si_{16.5}$ glass thin film, and I_r was varied by reading the camera multiple times at each probe position, which we call "pixel cycling". The data were collected with 50 pixel cycles, and then averaged over 4, 8, 12, 16, 25, 30 and 50 cycles to vary I_r. The individual END patterns were thresholded to remove dark counts before summation, but not processed with an electron counting filter. The summed image was converted to electron counts by dividing by the mean number of counts per incident electron for the camera. The scan step size was large compared to the probe diameter so the spatial samples are independent for later averaging. To correct for the Poisson noise using Eq. 3, the ring variance was estimated using $V_r = \langle I^2 \rangle / \langle I \rangle^2 - 1 - 1/I_r$.

The experimental $S(2)$ of $Pd_{77.5}Cu_6Si_{16.5}$ in Figure 3 diverges at low I_r, similar to simulated results in Figure 2. By using the same definition of the mean ring intensity threshold discussed earlier, after noise correction, I_r larger than ~ 2.2 electron per pixel is found to give less than 5% deviation of $S(n)$ from S_0. Thresholds at other conditions can be found in Table 1. Thresholds before noise correction are much larger for the $Pd_{77.5}Cu_6Si_{16.5}$ experiment data comparing to that for the $Al_{94}Sm_6$ simulation. This is because the ring variance measured from $Pd_{77.5}Cu_6Si_{16.5}$ experiment is much smaller ($V_r = 0.239$ for data with the highest I_r). The thresholds obtained after noise correction coincides between $Pd_{77.5}Cu_6Si_{16.5}$ experiment and $Al_{94}Sm_6$ simulation within experimental error (see Table 1), which suggests that the counting statistics for symmetry coefficient after noise correction is potentially structure-invariant, and the thresholds obtained here can serve as a guideline for future experiments.

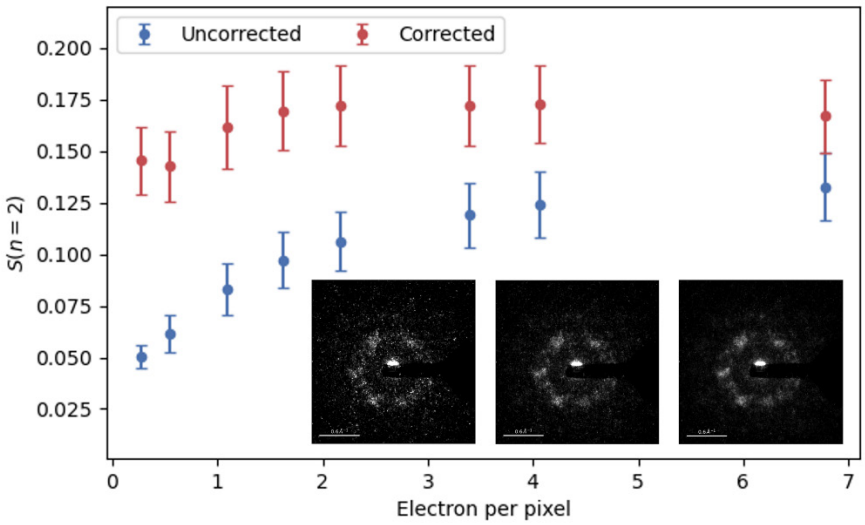

Figure 3. Spatial averaged $S(2)$ of $Pd_{77.5}Cu_6Si_{16.5}$ glass thin film at different mean ring intensity before (blue) and after (red) noise correction. The inset images are examples of summed patterns over different pixel cycles at the same spatial position. Scale bars are 0.6 $Å^{-1}$.

Another approach to adjusting I_r is to change the effective size of a detector pixel in reciprocal space by either changing the camera length or post-acquisition binning of the END patterns. This practice, however, is limited by the effect of low k sampling on symmetry coefficient. Lower k-sampling of speckles leads to weaker variability of the intensity in the diffraction ring. Additionally, the ability to resolve the angular position of the speckles is reduced. The effect of k-sampling on correlation symmetry analysis was studied by calculating averaged $S(n)$'s of $Al_{94}Sm_6$ model from simulated datasets with different binning factors, resulting in pixel sizes from 0.00346 $Å^{-1}$ to 0.0553 $Å^{-1}$. As the pixel size increases, both V_r and $S(n)$

decrease. In other words, the symmetry information becomes partially lost when the speckle size in pixels becomes too small. From the simulated dataset, $S(n)$ reached a plateau for the speckles 15 pixels or more in diameter. This level of k-sampling can be hard to reach while maintaining the necessary I_r, so some reduction in $S(n)$ due to poor k-sampling may be required for certain experiments. As long as the pixel sampling per speckle is kept constant, the $S(n)$ from different experiments can be reliably compared.

Probe current is another parameter that determines I_r. However, increasing the probe current at fixed aperture size and probe convergence angle means reducing the spatial coherence of the probe, since the source area is proportional to the probe current [29]. Fig. 4 shows V_r as a function of spot size from the 20 nm $Pd_{77.5}Cu_6Si_{16.5}$ glass sample. V_r is averaged over the same k window used to calculate symmetry coefficients, and smaller spot number means higher probe current. The mean ring intensity is kept consistent at different spot sizes by adjusting the detector acquisition time. As the probe current increases, the magnitude of V_r decreases substantially. A 4-fold increase of probe current from 1.6 to 6.4 pA leads to a reduction of V_r by ~ 65%. (A brighter source would provide more current at the same degree of spatial coherence.)

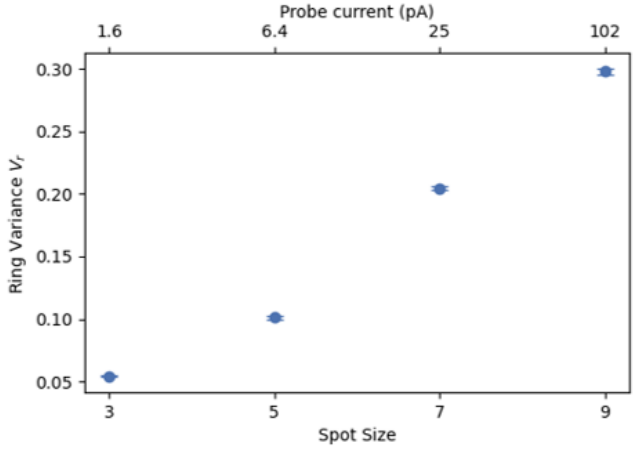

Figure 4. Spatial averaged V_r of $Pd_{77.5}Cu_6Si_{16.5}$ glass thin film sample under probes with different spot sizes. V_r is averaged over k range from 0.4 $Å^{-1}$ to 0.5 $Å^{-1}$. Electron intensities collected at each spot size are kept constant by changing the detector frame rate.

The interpretability of the structural symmetries in the END patterns also depends on the probe-sample interaction volume, which is in turn controlled by the sample thickness and probe diameter. The probability of the pattern containing speckles from more than one cluster of atoms and the probability of multiple electron scattering both increase with increasing volume, with the potential to create complicated and sometimes misleading correlations [30]. While correlation symmetry analysis reduces this effect compared to other methods [17], Figure 5 demonstrates that it is still preferable to reduce the interaction volume by either decreasing the probe size or preparing thinner samples. We use the ratio between structural even symmetry coefficients and potentially non-structural odd symmetry coefficients as a metric to judge the interpretability of the experimental data. S_{even} is defined as the average of 2-, 4-, 6- and 10-fold symmetry coefficients, and S_{odd} is defined as the average of 7- and 9- fold symmetry coefficients. For samples both 10 nm and 20 nm thick, $S_{\mathrm{even}}/S_{\mathrm{odd}}$ increases with decreasing probe size. At fixed probe size, $S_{\mathrm{even}}/S_{\mathrm{odd}}$ is consistently larger for the thinner sample. In general, a thinner sample is better for high quality correlation symmetry mapping, but determining the optimum probe size is more complicated. While a smaller probe gives a smaller interaction volume, the larger convergence angle also leads to more coherent interference

of overlapping speckles, which in previous simulations potentially diminished angular correlations in END patterns [19]. Thus, a probe size similar to the average size of the clusters is preferred for discerning local clusters from structural symmetries in END patterns [31]. Here the minimum probe size used in Fig.5 was ~ 0.6 nm, which is slightly smaller than the average size of the clusters measured from the mapping experiment discussed later.

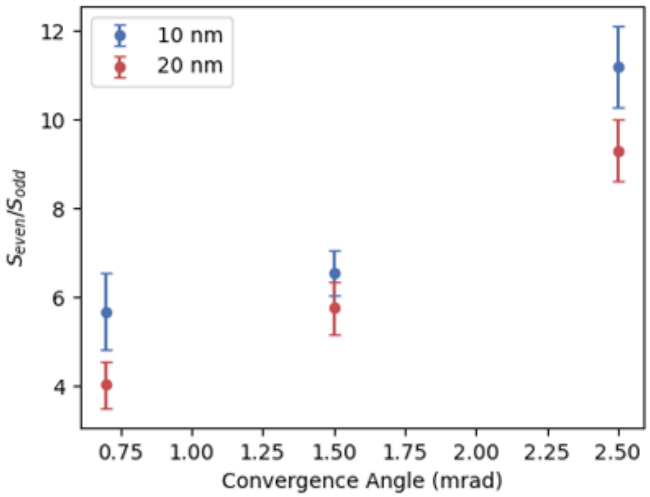

Figure 5. Ratio between structural S_{even} and non-structural S_{odd} versus probe convergence angle for $Pd_{77.5}Cu_6Si_{16.5}$ glass thin film samples with thicknesses of 10 nm (blue) and 20 nm (red). Error bars are calculated from the standard deviations of structural even symmetry coefficients and non-structural odd symmetry coefficients following the propagation of uncertainty.

Based on the results from Figures 2 through 5, we can establish an envelope of operating conditions for quantitatively reliable fast 4D STEM symmetry mapping experiments. With Poisson noise correction using Eq. 3, the mean ring intensity should be 2.2 electrons per pixel or larger. The mean ring intensity per pixel can be controlled by (1) the probe current, (2) the detector frame rate, and (3) the size of the pixels in reciprocal space. The pixel size is in turn controlled by the camera length and post-acquisition binning. Intensity can be increased by increasing the probe current, but that reduces the probe coherence and thus reduces the signal. In general, high coherence, low current probes are preferable. The minimum reciprocal space pixel size is set by the k-sampling requirement, which suggests that the speckles be 15 pixels or more in diameter. Detector frame rate is the most freely adjustable parameter and should be tailored for the needs of individual experiments.

Experiments with different objectives will require different combinations within the operating envelope. For example, a typical large area 4D STEM symmetry mapping experiment on a metallic glass sample should use an intermediate to slow frame rate, limited by the need to avoid saturating the detector, the total acquisition time limit and the scanning size, to allow a small probe current. On the other hand, the same experiment on a beam sensitive material needs to use a faster frame rate set by the dose limit of the sample. In this case, a smaller camera length or more post-acquisition binning is needed to maintain the required mean ring intensity. An *in-situ* time-resolved 4D STEM experiment requires an ultrafast frame rate for the time resolution, which in turn requires a larger probe current and large k pixels to maintain ring intensity. The S_n signal will be reduced, but not made noisy or subject to artifacts. A few examples sets of parameters for our Titan STEM are summarized in Table 2. It is worth noting that the experimental parameters studied

here are not exhaustive. Other factors such as the size and shape of a beam stop, energy filtering, and electron counting filter can also influence the correlation symmetry analysis.

Table 2. Examples of experimental parameters on a FEI Titan G2 microscope mounted with a DE-Celeritas detector for different types of 4D-STEM symmetry mapping experiments.

Experiment	Spot size / probe current	Camera length / detector area / *k* pixel size	Detector frame rate
Large area 4D STEM	7 / 6.4 pA	48 mm / 256 by 256 / 0.00979 $Å^{-1}$	1000 fps
Large area 4D STEM for beam sensitive materials	11 / 0.6 pA	1700 mm (EFSTEM) / 256 by 256 / 0.00495 $Å^{-1}$	8000 fps
In-situ time-resolved 4D STEM	5 / 25 pA	38 mm / 256 by 128 / 0.01239 $Å^{-1}$	8000 fps

3.3 Example Symmetry Mapping Experiment

Figure 6 shows the average symmetry coefficients and symmetry maps from a symmetry mapping experiment on a 10 nm thick $Pd_{77.5}Cu_6Si_{16.5}$ thin film sample. A 1000 by 1000 spatial pixel 4D STEM data set was collected from a 62 by 62 nm sample area at 1000 fps, using a probe current of 6.4 pA, a convergence angle of 2.51 mrad and a camera length that produces 20 pixels per speckle diameter. The mean ring intensity was 2.72 electrons per pixel mean ring, well above the threshold for 5% error after noise correction.

Figure 6a shows the noise corrected pattern averaged symmetry coefficient with positive truncation. The 7- and 9-fold non-structural odd symmetries are almost completely suppressed. Figure 6b-f show the 2-, 4-, 6-, 8- and 10-fold symmetry maps. The intensities are positive truncated and the color scale is normalized by the maximum value for each map. These maps display the spatial distributions of on-axis local clusters with different symmetry orders. Clusters with higher intensity indicate stronger symmetric diffraction, which can arise from the cluster orientation, less distortion in the atomic arrangement, higher volume fraction of the cluster in the interaction volume, or more random structure in rest of the volume. The 2-fold map has the most features because all structural even symmetries must contain 2-fold symmetry. It can be viewed as the map of all diffracting ordered local clusters regardless of configuration detail. The 4-fold map can be treated as the crystal-like cluster map, and the 10-fold map can be treated as the icosahedral-like cluster map. The 6-fold map has contributions from crystal-like and icosahedral-like packing arrangements, both of which have 6-fold symmetric diffraction patterns orientations. The 8-fold map comes from 8-fold symmetry, which is not crystallographic.

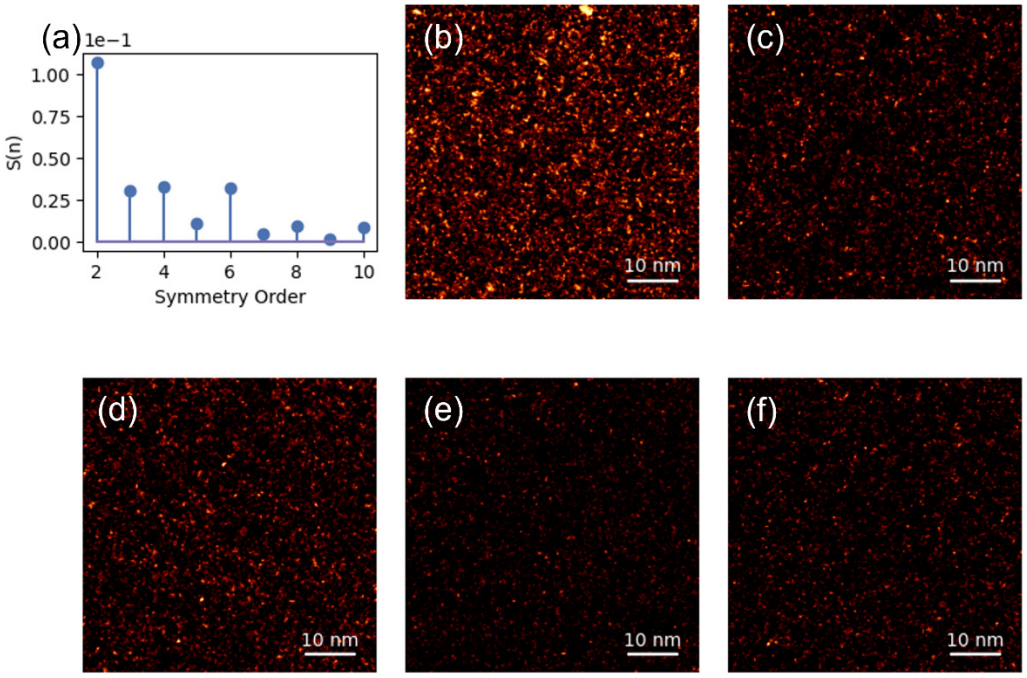

Figure 6. (a) Pattern averaged positive truncated symmetry coefficients calculated from a large area 4D STEM experiment on a $Pd_{77.5}Cu_6Si_{16.5}$ thin film sample; (b) 2-fold, (c) 4-fold, (d) 6-fold, (e) 8-fold, and (f) 10-fold symmetry maps from the same sample area. Intensities are positive truncated and scaled by the maximum value of each map.

We have used a Laplacian of Gaussian (LoG) blob detection filter implemented in scikit-image [32] on the symmetry maps to identify the size, position, and intensity of local diffracting clusters. A threshold of 0.025 was used to exclude unmeaningful correlations [17], and the size of the clusters was determined as the full-width half maximum of a Gaussian kernel which gave the maximum correlation with the cluster as a function of the Gaussian standard deviation. Figure 7a shows an enlarged area of 2-fold symmetry map shown in Fig. 6b overlaid with cluster objects. (The circles are slightly larger than the actual cluster sizes so they do not block features in the symmetry map.) The clusters are one half to a few nanometers in diameter, consistent with previous experimental results on other metallic glasses measured by either angular correlation [20] or fluctuation microscopy [28,33]. Figure 7b shows the histogram of the total number of clusters detected in the symmetry maps with different orders. The populations of 2-, 3-, 4- and 6-fold clusters are significantly higher than the populations of 5- 8-, and 10-fold clusters. 7- and 9-fold clusters are scarce. This is consistent with the pattern averaged correlation symmetry profile shown in Figure 6a.

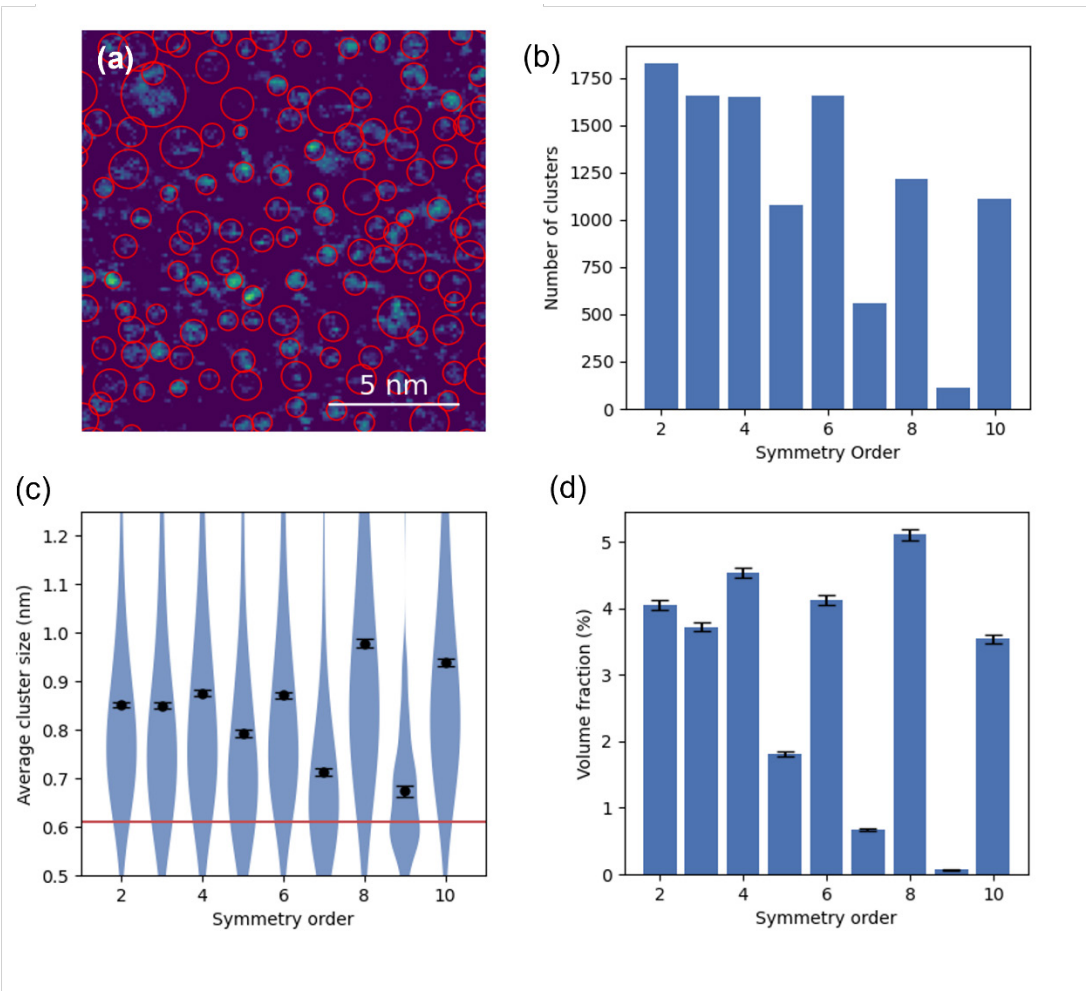

Figure 7. (a) Enlarged area of the 2-fold symmetry map shown in Fig. 6b overlaid with cluster object detected; (b) histogram of total number of clusters; (c) violin plot of the cluster size distributions and average cluster sizes (black circles); and (d) histogram of the volume fraction of the clusters with different orders. The circles in (a) are larger than the cluster sizes. The red line in (c) marks the probe size, and error bars are one standard deviation of the mean. Error bars in (d) are calculated from size measurement uncertainty (0.75 pixel) following the propagation of uncertainty.

Figure 7c shows the size distributions and the average sizes of clusters with different rotational symmetries. Only clusters with sizes larger than 0.25 nm (~ one interatomic distance) were used to calculate the average size. The even order clusters, (2, 4-, 6- 8- and 10-fold) have very similar shaped distributions and average diameters significantly larger than the probe size. Most of the cluster are around two to five interatomic distances, implying that both SRO and MRO clusters are captured in the mapping experiment. The average sizes of 7- and 9-fold symmetry clusters are close to the probe size, and a large fraction of size distribution is smaller than the probe size. Small size is reasonable since many of the odd-symmetry clusters arise from non-structural sources, like chance correlations amongst speckles diffracted from different but overlapping structures.

The 8- and 10-fold symmetries are not crystallographically allowed. The origin of the 8-fold correlation could be related to the 45° rotation between the two rings of four atoms in the bicapped square antiprism

configuration (BSAP) with Voronoi index <0,2,8,0>, which is thought be one of the predominant atomic packing environments in Pd-Si-based metallic glasses [34–36]. The 10-fold clusters most likely arise from icosahedral arrangements of atoms with Voronoi indices like <0 0 12 0> with 5-fold real-space symmetry Friedel doubled to 10-fold in diffraction. The mean size of the 8- and 10-fold clusters is larger than the crystallographically-allowed 2-, 4-, and 6-fold clusters. Glass forming ability of different alloys has been attributed to the thermodynamic stability of crystal-like and non-crystal-like structures. $Pd_{77.5}Cu_6Si_{16.5}$ is a good glass former, so these result may indicate that the size of crystal-like vs non-crystal-like structures may also reflect glass forming ability.

Figure 7d shows a rough upper bound estimate of the volume densities of these clusters, based on assuming a spherical shape for all clusters and an average Bragg acceptance angle of 10° [13]. The estimate is an upper bound because the acceptance angle about the zone axis configuration for higher symmetries will be smaller than the Bragg acceptance angle estimate in Ref. [13]. 4-fold clusters have the highest volume fraction of 4.5 ± 0.1 % (not including cluster with higher 8-fold symmetry). 2-, 6-fold clusters are both lower at around 4.1 ± 0.1 %. 10-fold clusters have the lowest volume fraction among even symmetries at 3.5 ± 0.1 %. The uncertainties quoted here reflect the random uncertainties from the sample thickness estimate and the counting statistics of clusters in the data. Systematic errors arising from the diffraction acceptance angle for the various clusters will be non-random and may be significantly larger than the random uncertainties. Material- and structure-specific models for diffraction acceptance of various clusters is required to obtain a more accurate estimate of cluster volume fractions.

Modelling suggests that PdSi glasses have high fraction of 9-coordinated tricapped trigonal prisms (TTPs) with Voronoi index <0,3,6,0> and 10-coordinated BSAPs [35], both centered by Si atoms. Cu atoms substitute at Pd sites, and they are thought to bring TTPs closer to each other, while leaving the structure motif largely unchanged [37]. An ideal TTP has one 3-fold rotational symmetry axis and an ideal BSAP has one 4-fold rotational symmetry axis. The similar magnitude of pattern averaged $S(4)$ and $S(6)$ in Fig. 6a as well as similar number of 4- and 6-fold clusters in Fig. 7b confirm the coexistence of these two motifs in the structure. The higher volume fraction of 4-fold clusters compared to that of 6-fold clusters suggests the structure may have a higher BSAP fraction. The intermediate number of 10-fold cluster suggests the existence of icosahedral-like packing. An ideal icosahedral has 6 5-fold symmetry axes, therefore the volume fraction of 10-fold clusters shown in Fig. 7d is overestimated, since the multiplication of symmetry axes was not accounted for.

Previous VR-FEM studies measured the MRO cluster sizes of about 2 nm to 4 nm for Cu-Zr-based metallic glasses [33,38], and about 1 nm to 1.5 nm for a Pd-Ni-P glass [39]. Angular power spectrum studies on Zr-Cu/Co-based glasses obtained MRO cluster sizes of 1 to 1.5 nm [40]. Here, we measured sizes range from 0.6 to 1.3 nm with means of ~ 0.8 nm for MRO/SRO clusters with different types of symmetries in Pd-Si based glass, as shown in Fig. 7c. This might suggest that MRO clusters in Zr-late transition metal-based glasses are larger than Pd-non-metal-based glasses. However, these results are not strictly comparable as the quantities and objects being measured are different between VR-FEM and angular power spectrum or symmetry mapping. The beam sizes used in the various experiments are also not the same. In addition, symmetry coefficients are calculated from the second power (autocorrelation) of the intensity profile, which will tend to reduce the size compared to other measures that are linear in the intensity. The volume fraction measured here is comparable to the values reported from the angular power spectrum studies on Zr-Co-Al glass [20]. Therefore, symmetry mapping experiment holds great potential as a non-model-dependent alternative to VR-FEM and less and less artifact-prone alternative to angular power spectrum in studying the correlation between structural heterogeneities and mechanical properties or glass forming abilities [41,42].

Figure 8a is an enlarged area of the 7-fold symmetry map from the same data set showing an example of diffraction from overlapping clusters creating non-structural symmetry. Green and orange circles mark the positions of clusters in the 4- and 6-fold symmetry maps. They overlap with the red circle which marks the position of a 7-fold symmetry cluster. The two inset images on the left show the spatial averaged diffraction patterns of the two overlapping 4- and 6-fold clusters, with the speckles contributing to their symmetry coefficients circled. The inset image on the right is the spatial averaged pattern for the 7-fold cluster, which can be deconstructed into speckles that are also present in the 4-fold and 6-fold cluster diffraction patterns. Therefore, in this overlapping region, the electron beam traverses through the sample and encounters the 4-fold and 6-fold clusters at different positions in the thickness. Due to the relative rotation between these two clusters, part of a 7-fold symmetric ring of speckles is produced. There is no seven-fold symmetric arrangement of atoms in the sample.

A more systematic analysis shows that most of the observed 7- and 9-fold symmetric clusters arise from these kinds of random overlaps. We define a cluster as "non-overlapping" if more than 50% of the spatial pixels it contains are not part of a cluster with any other symmetry. This ensures that the non-overlapping clusters cannot be a result of half symmetry elements (*e.g.,* 3-fold from 6-fold) or random overlaps. Figure 8b shows that fraction of 2-fold symmetry clusters that are non-overlapping is larger than 25%. 3-, 4-, 5-, 6- and 10-fold symmetries have non-overlapping fractions between 10% and 20%. 7- and 9-fold symmetries have non-overlapping fractions below 10%.

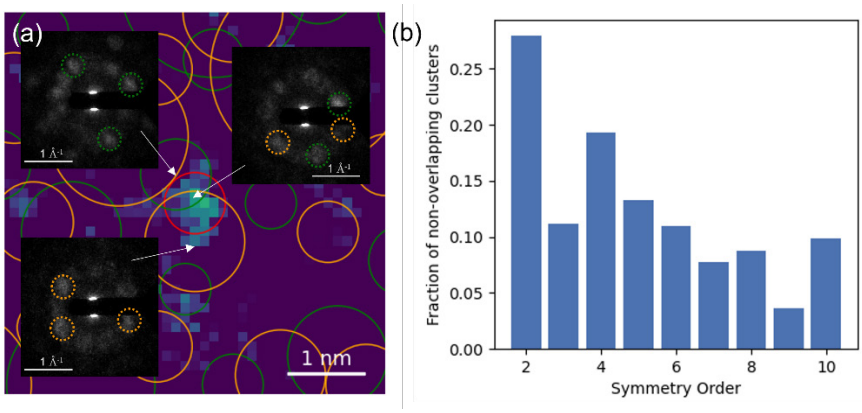

Figure 8. (a) Enlarged area of the 7-fold symmetry map around a 7-fold cluster (red) overlaid with 4-fold (green), 6-fold (orange) cluster positions from the respective maps. Inset images show spatial averaged pattern from the three clusters marked by the white arrows; (b) fractions of non-overlapping clusters for different symmetry orders.

Figure 9 shows the 2D spatial correlation function of the clusters with different symmetries calculated from the symmetry maps. The correlation function is defined as $C_2(r) = \langle S(\boldsymbol{r}')S(\boldsymbol{r}'+\boldsymbol{r})\rangle_{\boldsymbol{r}'}/\langle S(\boldsymbol{r}')\rangle^2 - 1$, where $S(\boldsymbol{r})$ is the intensity of symmetry maps. The C_2's show peaks at non-zero distance, indicating spatial correlations among clusters. 2-, 4-, 6- and 10-fold clusters show peaks at distances larger than 2 nm, suggesting the existence of ordered arrangement of TTPs, BSAPs and icosahedra at larger length scales, potentially corresponds to the connected network SROs structures found previously in metallic glasses from both experiments [6] and simulations [43–45]. All four structural even symmetries have different shapes of C_2's with some peaks coinciding, suggesting different spatial correlations exists for different types of clusters but some of which originate from the same ordering. Measuring spatial correlations from 4D STEM symmetry mapping experiments have potential for studying larger length scale structural features in glasses

and supercooled liquids such as chain-like connectivity of SRO clusters [46] and spatial heterogeneities [47].

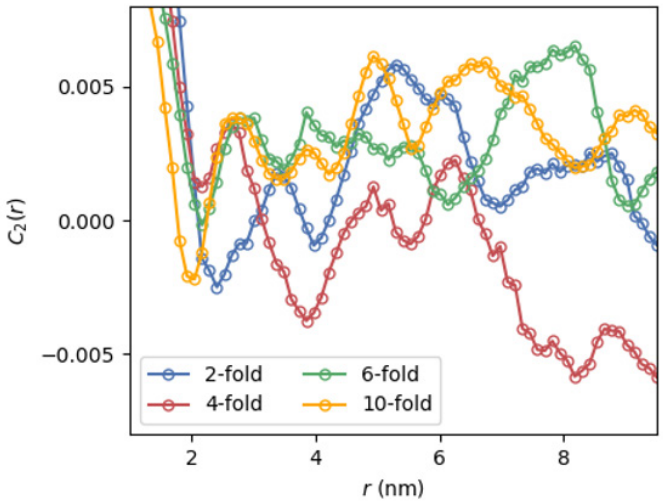

Figure 9. 2D correlation functions of the symmetry maps at different symmetry orders.

4. Summary

Symmetry coefficient analysis of large, densely sampled 4D STEM data sets from amorphous materials can characterize the prevalence of different forms of rotationally symmetric local structures, including the size and density of local clusters with different symmetry. Simulated END dataset link the symmetry coefficients to the local atomic structure in atomistic models. Poisson noise leads to a minimum electron intensity requirement to obtain a well-converged estimate symmetry coefficients, although correcting for the noise-induced reduction in $S(n)$ decreases the minimum electron intensity threshold in both simulation and experiment. Symmetry coefficients also require sufficient sampling of each speckle in the diffraction pattern and benefit from high probe coherence. An operating parameter envelope for the electron intensity per pixel, the probe coherence, and the reciprocal space sampling to produce high quality correlation symmetry analysis and mapping with statistical significance was presented. Non-structural odd symmetries largely arise from the overlap of diffraction from separate clusters of atoms through the sample thickness. This effect can be reduced by probing a smaller sample volume by using a thinner sample or a smaller probe. An example large area 4D STEM symmetry mapping experiment on a Pd-based metallic glass thin film demonstrates the ability to analyze the types, sizes, volume fraction and spatial correlation of local atomic clusters as a function of their rotational symmetry. The results suggest the coexistence of both TTPs and BSAPs in the sample structure. These SROs potentially connect into networks and form MROs with sizes ranges from 0.6 to 1.3 nm.

Appendix A: Poisson noise

Symmetry coefficients sample the Pearson's correlation of the intensity at different angles. The Pearson's correlation is $\rho = \left(\langle I_i I_j \rangle - \langle I_i \rangle^2\right) / \left(\langle I_i^2 \rangle - \langle I_i \rangle^2\right)$, where I_i is the intensity in each pixel on a ring segment that share the same magnitude of k, and $I_{j=i+d}$ is the intensity of the pixel that is d pixels apart from i in that ring. We decompose the intensity as $I_i = I_0 + S_i + n_i$, where I_0 is the ring mean intensity, S_i is the deviation from I_0, and n_i is the Poisson noise intensity. The terms in the Pearson's correlation become

$$\langle I_i I_j \rangle = \frac{1}{N}\sum_i \left(I_0^2 + S_i S_j\right), \tag{A1}$$

$$\langle I_i^2 \rangle = \frac{1}{N}\sum_i \left(I_0^2 + S_i^2 + n_i^2\right), \tag{A2}$$

assuming that S_i and n_i are uncorrelated and n_i and n_j are uncorrelated. Substituing into the Pearson's correlation definition gives

$$\rho = \frac{\langle S_i S_j \rangle}{\langle S_i^2 \rangle + \langle n_i^2 \rangle}. \tag{A3}$$

For Poisson noise of electron detection, the noise variance equals to mean electron intensity, so $\langle n_i^2 \rangle = I_0$. Thus Eq. A3 can be written as

$$\rho = \frac{\langle S_i S_j \rangle}{\langle S_i^2 \rangle + I_0} = \frac{\langle S_i^2 \rangle}{\langle S_i^2 \rangle + I_0} \cdot \frac{\langle S_i S_j \rangle}{\langle S_i^2 \rangle}. \tag{A4}$$

The second fraction term is the Pearson's correlation without noise ρ_0 as defined by Eq. 1, giving

$$\rho = \frac{1}{1 + I_0/\langle S_i^2 \rangle} \cdot \rho_0. \tag{A5}$$

Consider the ring variance $V_r = \langle S_i^2 \rangle / I_0^2$, as defined in ref [28]. Eq. A5 can then be written as

$$\rho = \frac{1}{1 + 1/I_0 V_r} \cdot \rho_0. \tag{A5}$$

Following Eq.2, this gives us the functional form of Poisson noise influence on symmetry coefficients defined by Eq. 3.

Acknowledgements

This work was supported by the Wisconsin MRSEC (DMR-1720415).

Data and Software Availability

The datasets generated and analyzed in this work are available at [48]. The symmetry coefficient analysis and mapping used here are implemented in the open source pyxem package for 4D STEM, available at [26].

References

[1] Y.Q. Cheng, E. Ma, Atomic-level structure and structure-property relationship in metallic glasses, Progress in Materials Science. 56 (2011) 379–473. https://doi.org/10.1016/j.pmatsci.2010.12.002.

[2] F.C. Frank, J.S. Kasper, Complex alloy structures regarded as sphere packings. II. Analysis and classification of representative structures, Acta Crystallographica. 12 (1959) 483–499. https://doi.org/10.1107/S0365110X59001499.

[3] D.R. Nelson, F. Spaepen, Polytetrahedral Order in Condensed Matter, in: H. Ehrenreich, D.B.T.-S.S.P. Turnbull (Eds.), Superconductivity Quasicrystals Two Dimensional Physics, Academic Press, 1989: pp. 1–90. https://doi.org/10.1016/S0081-1947(08)60079-X.

[4] W.G. Stratton, J. Hamann, J.H. Perepezko, P.M. Voyles, X. Mao, S. V. Khare, Aluminum nanoscale order in amorphous Al92 Sm8 measured by fluctuation electron microscopy, Applied Physics Letters. 86 (2005) 1–3. https://doi.org/10.1063/1.1897830.

[5] M. Li, C.Z. Wang, S.G. Hao, M.J. Kramer, K.M. Ho, Structural heterogeneity and medium-range order in Zrx Cu100-x metallic glasses, Physical Review B - Condensed Matter and Materials Physics. 80 (2009). https://doi.org/10.1103/PhysRevB.80.184201.

[6] J. Hwang, Z.H. Melgarejo, Y.E. Kalay, I. Kalay, M.J. Kramer, D.S. Stone, P.M. Voyles, Nanoscale structure and structural relaxation in Zr 50Cu 45Al 5 bulk metallic glass, Physical Review Letters. 108 (2012). https://doi.org/10.1103/PhysRevLett.108.195505.

[7] P. Zhang, Z. Wang, J.H. Perepezko, P.M. Voyles, Vitrification, crystallization, and atomic structure of deformed and quenched Ni60Nb40 metallic glass, Journal of Non-Crystalline Solids. 491 (2018) 133–140. https://doi.org/10.1016/j.jnoncrysol.2018.04.005.

[8] P. Zhang, J.J. Maldonis, M.F. Besser, M.J. Kramer, P.M. Voyles, Medium-range structure and glass forming ability in Zr-Cu-Al bulk metallic glasses, Acta Materialia. 109 (2016) 103–114. https://doi.org/10.1016/j.actamat.2016.02.006.

[9] Y.Q. Cheng, E. Ma, H.W. Sheng, Alloying strongly influences the structure, dynamics, and glass forming ability of metallic supercooled liquids, Applied Physics Letters. 93 (2008) 11–13. https://doi.org/10.1063/1.2987727.

[10] Y.C. Hu, F.X. Li, M.Z. Li, H.Y. Bai, W.H. Wang, Five-fold symmetry as indicator of dynamic arrest in metallic glass-forming liquids, Nature Communications. 6 (2015) 6–13. https://doi.org/10.1038/ncomms9310.

[11] Y.Q. Cheng, H.W. Sheng, E. Ma, Relationship between structure, dynamics, and mechanical properties in metallic glass-forming alloys, Physical Review B - Condensed Matter and Materials Physics. 78 (2008) 1–7. https://doi.org/10.1103/PhysRevB.78.014207.

[12] P.M. Voyles, D.A. Muller, Fluctuation microscopy in the STEM, Ultramicroscopy. 93 (2002) 147–159. https://doi.org/https://doi.org/10.1016/S0304-3991(02)00155-9.

[13] W.G. Stratton, P.M. Voyles, A phenomenological model of fluctuation electron microscopy for a nanocrystal/amorphous composite, Ultramicroscopy. 108 (2008) 727–736. https://doi.org/10.1016/j.ultramic.2007.11.004.

[14] J.M. Cowley, Electron nanodiffraction methods for measuring medium-range order, Ultramicroscopy. 90 (2002) 197–206. https://doi.org/10.1016/S0304-3991(01)00130-9.

[15] A.C.Y. Liu, G.R. Lumpkin, T.C. Petersen, J. Etheridge, L. Bourgeois, Interpretation of angular symmetries in electron nanodiffraction patterns from thin amorphous specimens, Acta Crystallographica Section A: Foundations and Advances. 71 (2015) 473–482. https://doi.org/10.1107/S2053273315011845.

[16] E.D. Bøjesen, T.C. Petersen, A. V Martin, M. Weyland, A.C.Y. Liu, Statistical measures of angular correlations in amorphous materials from electron nano-diffraction in the scanning/transmission

electron microscope, Journal of Physics: Materials. 3 (2020) 044002. https://doi.org/10.1088/2515-7639/aba820.

[17] S. Huang, C. Francis, J. Ketkaew, J. Schroers, P.M. Voyles, Correlation symmetry analysis of electron nanodiffraction from amorphous materials, Ultramicroscopy. 232 (2022) 113405. https://doi.org/https://doi.org/10.1016/j.ultramic.2021.113405.

[18] M. Krajnak, J. Etheridge, A symmetry-derived mechanism for atomic resolution imaging, (2019) 1–7.

[19] A.C.Y. Liu, M.J. Neish, G. Stokol, G.A. Buckley, L.A. Smillie, M.D. De Jonge, R.T. Ott, M.J. Kramer, L. Bourgeois, Systematic mapping of icosahedral short-range order in a melt-spun Zr 36Cu64 metallic glass, Physical Review Letters. 110 (2013) 1–5. https://doi.org/10.1103/PhysRevLett.110.205505.

[20] S. Im, Z. Chen, J.M. Johnson, P. Zhao, G.H. Yoo, E.S. Park, Y. Wang, D.A. Muller, J. Hwang, Direct determination of structural heterogeneity in metallic glasses using four-dimensional scanning transmission electron microscopy, Ultramicroscopy. 195 (2018) 189–193. https://doi.org/10.1016/j.ultramic.2018.09.005.

[21] D. Chatterjee, J. Wei, A. kvit, B. Bammes, B. Levin, R. Bilhorn, P. Voyles, An Ultrafast Direct Electron Camera for 4D STEM, Microscopy and Microanalysis. 27 (2021) 1004–1006. https://doi.org/DOI: 10.1017/S1431927621003809.

[22] P.M. Pelz, I. Johnson, C. Ophus, P. Ercius, M.C. Scott, Real-Time Interactive 4D-STEM Phase-Contrast Imaging From Electron Event Representation Data: Less computation with the right representation, IEEE Signal Processing Magazine. 39 (2022) 25–31. https://doi.org/10.1109/MSP.2021.3120981.

[23] C. Zhang, J. Feng, L.R. DaCosta, P.M. Voyles, Atomic resolution convergent beam electron diffraction analysis using convolutional neural networks, Ultramicroscopy. 210 (2020) 112921. https://doi.org/10.1016/j.ultramic.2019.112921.

[24] V. Jambur, C. Tangpatjaroen, J. Xi, J. Tarnsangpradit, M. Gao, H. Sheng, J.H. Perepezko, I. Szlufarska, Effects of minor alloying on the mechanical properties of Al based metallic glasses, Journal of Alloys and Compounds. 854 (2021). https://doi.org/10.1016/j.jallcom.2020.157266.

[25] L. Rangel DaCosta, H.G. Brown, P.M. Pelz, A. Rakowski, N. Barber, P. O'Donovan, P. McBean, L. Jones, J. Ciston, M.C. Scott, C. Ophus, Prismatic 2.0 – Simulation software for scanning and high resolution transmission electron microscopy (STEM and HRTEM), Micron. 151 (2021) 103141. https://doi.org/https://doi.org/10.1016/j.micron.2021.103141.

[26] D. Johnstone, P. Crout, M. Nord, C. Francis, J. Laulainen, S. Høgås, E. Opheim, B. Martineau, T. Bergh, E. Prestat, N. Cautaerts, S. Smeets, A. Ross, J. Broussard, H.W. Ånes, S. Collins, T. Furnival, D. Jannis, I. Hjorth, M. Danaie, A. Herzing, E. Jacobsen, T. Poon, T. Doherty, S. Huang, J. Morzy, A. Iqbal, T. Ostasevicius, M. von Lany, R. Tovey, pyxem/pyxem: pyxem 0.14.1, (2022). https://doi.org/10.5281/ZENODO.6505200.

[27] A. Hirata, P. Guan, T. Fujita, Y. Hirotsu, A. Inoue, A.R. Yavari, T. Sakurai, M. Chen, Direct observation of local atomic order in a metallic glass, Nature Materials. 10 (2011) 28–33. https://doi.org/10.1038/nmat2897.

[28] T.L. Daulton, K.S. Bondi, K.F. Kelton, Nanobeam diffraction fluctuation electron microscopy technique for structural characterization of disordered materials-Application to Al88-xY7Fe5Tix metallic glasses, Ultramicroscopy. 110 (2010) 1279–1289. https://doi.org/10.1016/j.ultramic.2010.05.010.

[29] F. Yi, P. Tiemeijer, P.M. Voyles, Flexible formation of coherent probes on an aberration-corrected STEM with three condensers, Journal of Electron Microscopy. 59 (2010) 15–21. https://doi.org/10.1093/jmicro/dfq052.

[30] T. Sun, M.M.J. Treacy, T. Li, N.J. Zaluzec, J.M. Gibson, The importance of averaging to interpret electron correlographs of disordered materials, Microscopy and Microanalysis. 20 (2014) 627–634. https://doi.org/10.1017/S1431927613014116.

[31] A.C.Y. Liu, R.F. Tabor, L. Bourgeois, M.D. De Jonge, S.T. Mudie, T.C. Petersen, Probing local order in glasses from limited-volume electron and x-ray diffraction, Journal of Statistical Mechanics: Theory and Experiment. 2016 (2016). https://doi.org/10.1088/1742-5468/2016/05/054046.

[32] S. van der Walt, J.L. Schönberger, J. Nunez-Iglesias, F. Boulogne, J.D. Warner, N. Yager, E. Gouillart, T. Yu, the scikit-image contributors, scikit-image: image processing in Python, PeerJ. 2 (2014) e453. https://doi.org/10.7717/peerj.453.

[33] J. Hwang, P.M. Voyles, Variable resolution fluctuation electron microscopy on cu-zr metallic glass using a wide range of coherent stem probe size, Microscopy and Microanalysis. 17 (2011) 67–74. https://doi.org/10.1017/S1431927610094109.

[34] H.W. Sheng, W.K. Luo, F.M. Alamgir, J.M. Bai, E. Ma, Atomic packing and short-to-medium-range order in metallic glasses., Nature. 439 (2006) 419–25. https://doi.org/10.1038/nature04421.

[35] T. Ohkubo, Y. Hirotsu, Electron diffraction and high-resolution electron microscopy study of an amorphous (formula presented) alloy with nanoscale phase separation, Physical Review B - Condensed Matter and Materials Physics. 67 (2003) 1–9. https://doi.org/10.1103/PhysRevB.67.094201.

[36] J.J. Maldonis, P.M. Voyles, Local Structure Controlling the Glass Transition in a Prototype Metal-Metalloid Glass, ArXiv Preprint ArXiv:1901.07014. (2019).

[37] Y. Hayashi, H. Yamazaki, D. Ono, K. Masunishi, T. Ikehashi, Investigation of PdCuSi metallic glass film for hysteresis-free and fast response capacitive MEMS hydrogen sensors, International Journal of Hydrogen Energy. 43 (2018) 9438–9445. https://doi.org/10.1016/j.ijhydene.2018.03.149.

[38] S. Hilke, H. Rösner, D. Geissler, A. Gebert, M. Peterlechner, G. Wilde, The influence of deformation on the medium-range order of a Zr-based bulk metallic glass characterized by variable resolution fluctuation electron microscopy, Acta Materialia. 171 (2019) 275–281. https://doi.org/10.1016/j.actamat.2019.04.023.

[39] F.A. Davani, S. Hilke, H. Rösner, D. Geissler, A. Gebert, G. Wilde, Correlations between the ductility and medium-range order of bulk metallic glasses, Journal of Applied Physics. 128 (2020). https://doi.org/10.1063/5.0007564.

[40] S. Im, P. Zhao, G.H. Yoo, Z. Chen, G. Calderon, M.A. Gharacheh, O. Licata, B. Mazumder, D.A. Muller, E.S. Park, Y. Wang, J. Hwang, Structural Heterogeneity, Ductility, and Glass Forming Ability of Zr-Based Metallic Glasses, (2020). https://doi.org/10.48550/arxiv.2002.09347.

[41] S. Hilke, H. Rösner, G. Wilde, The role of minor alloying in the plasticity of bulk metallic glasses, (2020). https://doi.org/10.1016/j.scriptamat.2020.06.070.

[42] S. Im, Y. Wang, P. Zhao, G.H. Yoo, Z. Chen, G. Calderon, M. Abbasi Gharacheh, M. Zhu, O. Licata, B. Mazumder, D.A. Muller, E.S. Park, Y. Wang, J. Hwang, Medium-range ordering, structural heterogeneity, and their influence on properties of Zr-Cu-Co-Al metallic glasses, Physical Review Materials. 5 (2021) 115604. https://doi.org/10.1103/PhysRevMaterials.5.115604.

[43] M. Lee, C.M. Lee, K.R. Lee, E. Ma, J.C. Lee, Networked interpenetrating connections of icosahedra: Effects on shear transformations in metallic glass, Acta Materialia. 59 (2011) 159–170. https://doi.org/10.1016/j.actamat.2010.09.020.

[44] J. Ding, Y.Q. Cheng, E. Ma, Full icosahedra dominate local order in Cu64Zr34 metallic glass and supercooled liquid, Acta Materialia. 69 (2014) 343–354. https://doi.org/10.1016/j.actamat.2014.02.005.

[45] W. Lu, J.C. Tseng, A. Feng, J. Shen, Structural origin of the enhancement in glass-forming ability of binary Ni-Nb metallic glasses, Journal of Non-Crystalline Solids. 564 (2021) 120834. https://doi.org/10.1016/j.jnoncrysol.2021.120834.

[46] Y.Q. Cheng, E. Ma, H.W. Sheng, Atomic level structure in multicomponent bulk metallic glass, Physical Review Letters. 102 (2009) 1–4. https://doi.org/10.1103/PhysRevLett.102.245501.

[47] F. Zhu, A. Hirata, P. Liu, S. Song, Y. Tian, J. Han, T. Fujita, M. Chen, Correlation between Local Structure Order and Spatial Heterogeneity in a Metallic Glass, Physical Review Letters. 119 (2017) 1–6. https://doi.org/10.1103/PhysRevLett.119.215501.

[48] Huang. Shuoyuan, C. Francis, J. Sunderland, V. Jambur, I. Szlufarska, P.M. Voyles, Data for Large Area, High Resolution Mapping of Approximate Rotational Symmetries in a Pd77.5Cu6Si16.5 Metallic Glass Thin Film, Materials Data Facility. (2022). https://doi.org/10.18126/OQY3-1CYV.